ADVANCES IN ATMOSPHERIC SCIENCES, VOL. 43, JUNE 2026, 1144–1159

• Original Paper •

Local Evapotranspiration and Atlantic Decadal Variability Dominate the Humidification of Northwest China

Haipeng YU[1], Yongqi GONG[2], Jianping HUANG*[3], Qiang ZHANG[4], Yu REN[2], Hongyu LUO[1], Xin WANG[5], Shanling CHENG[1], and Jie ZHOU[2]

[1]*State Key Laboratory of Cryospheric Science and Frozen Soil Engineering, Nagqu Plateau Climate and Environment Observation and Research Station of Tibet Autonomous Region, Northwest Institute of Eco-Environment and Resources, Chinese Academy of Sciences, Lanzhou* 730000, *China*

[2]*College of Atmospheric Sciences, Lanzhou University, Lanzhou* 730000, *China*

[3]*Collaborative Innovation Center for Western Ecological Safety, Lanzhou University, Lanzhou* 730000, *China*

[4]*Lanzhou Institute of Arid Meteorology, CMA, Key Laboratory of Arid Climate Change and Reducing Disaster of Gansu Province/Key Open Laboratory of Arid Climate Change and Reducing Disaster, Lanzhou* 730020, *China*

[5]*College of Earth and Environmental Sciences, Lanzhou University, Lanzhou* 730000, *China*

(Received 26 July 2025; revised 22 October 2025; accepted 12 November 2025)

ABSTRACT

Over recent decades, Northwest China (NWC) has experienced significant precipitation enhancements under global warming. However, the moisture sources and mechanisms of the increased precipitation remain controversial, a critical issue for projecting the persistence of the humidification trend. Previous studies have generally attributed the increased precipitation to enhanced external moisture transport. Using the dynamic precipitation recycling model (DRM) combined with dynamic circulation diagnostic methods, this study systematically examined the physical mechanisms of summer precipitation changes in NWC during 1961–2020. The results reveal a precipitation trend shift that occurred around 1997, followed by a significant, 9.18% increase in precipitation after 1997. Although external moisture transport remains the dominant source of climatological precipitation, the decadal increase has been governed by local evapotranspiration, whose growth outpaced net external inflow changes. This change was primarily modulated by zonal planetary waves driven by the Atlantic Multidecadal Oscillation (AMO), placing NWC under anomalous ascent and moisture convergence. During 1998–2020, the AMO-induced circulation simultaneously reduced eastward moisture export from NWC and favored local recycling by enhancing evapotranspiration (+9.12%) and recycled precipitation (+10.51%). Temperature-induced cryospheric melt and vegetation recovery amplified the local evapotranspiration, allowing the recycled moisture component to become the primary contributor to the precipitation increase (78%), surpassing the contribution from advected moisture (22%). Despite recent wetting, water budget constraints acting in conjunction with a likely AMO phase transition imply that the humidification may not persist in the future.

Key words: Northwest China, drylands, water vapor source, moisture transport, humidification, interdecadal variability

Citation: Yu, H. P., and Coauthors, 2026: Local evapotranspiration and Atlantic decadal variability dominate the humidification of Northwest China. *Adv. Atmos. Sci.*, **43**(6), 1144−1159, https://doi.org/10.1007/s00376-025-5414-5.

Article Highlights:

- Northwest China's precipitation exhibited a significant increase of 9.18% after a notable shift around 1997.
- External moisture transport dominates the climatological precipitation of Northwest China.
- Intensified local evapotranspiration predominantly served as the primary water vapor source of enhanced precipitation.
- The AMO modulated precipitation enhancement by reducing the eastward export of moisture and enhancing local recycling.

1. Introduction

The IPCC Sixth Assessment Report (IPCC6) indicated that global mean precipitation has probably increased since the mid-20th century, with an accelerated intensification since the 1980s (IPCC, 2021). Rising surface temperatures have amplified surface evapotranspiration and the capacity of atmospheric moisture retention (Trenberth, 1998), but hydrological and climatic changes exhibited significant

* Corresponding author: Jianping HUANG
Email: hjp@lzu.edu.cn

regional variability (Li et al., 2019; Christidis and Stott, 2021). Northwest China (NWC), one of the driest regions in the world with an annual precipitation of approximately 150 mm (Zheng et al., 2017; Wang et al., 2020), has shifted from a "warm and dry" to a "warm and wet" climate state since the mid-1980s (Dore, 2005; Held and Soden, 2006; Hsu et al., 2011; Trenberth, 2011). This shift was characterized by increased frequency and intensity of heavy precipitation events (Shi et al., 2007; Zhang et al., 2019; Wang et al., 2020). In terms of seasonal distribution, summer precipitation dominated the significant seasonal changes, accounting for 60.2% of the annual precipitation. From 1961 to 2016, summer precipitation increased by 15.5 mm, representing 52.4% of the total increase (Li and Ma, 2018). Moreover, the summer precipitation changes showed significant regional variability, characterized by increases in western NWC and decreases in the eastern section (Chen and Dai, 2009; Wu et al., 2019; Liu et al., 2020b).

Numerous studies have focused on the hydrologic cycle and water vapor sources in NWC. First, Yao et al. (2020) and Wu et al. (2019) noted that the annual precipitation recycling rate has fluctuated by about 10%. Further research revealed that local evapotranspiration significantly contributes to precipitation in Xinjiang, particularly during the rainy season (37%; Zhang et al., 2022a) and extreme precipitation events (24.5%–30.2%; Hu et al., 2021). Studies by Wang et al. (2016) and Yao et al. (2020) indicated this contribution has recently increased. Secondly, the mid-latitude westerlies transport moisture from Central Asia, acting as a key external source and primary trigger for extreme precipitation (Zhou et al., 2019; Yao et al., 2021). An enhanced and northward-shifted westerly flow has also been linked to increased precipitation in NWC (Zhang et al., 2021). Finally, water vapor from the eastern Tibetan Plateau, eastern China, and the Indian Ocean entered NWC via the southern trough and East Asian Monsoon, further contributing to summer precipitation. A strong low-level easterly jet over the Hexi Corridor rapidly transported east-sourced moisture westward (Liu et al., 2020a; Chen et al., 2021b), while the interaction between the southern westerly trough and East Asian Monsoon transported Indian Ocean moisture westward, further intensifying precipitation (Yang et al., 2019; Zhang et al., 2022b).

Over recent decades, the increased precipitation in NWC showed a significant association with interconnected atmospheric and oceanic changes that enhance moisture transport (Chen and Zhai, 2014; Mattingly et al., 2016; Zhou and Zhai, 2016; Wang et al., 2022). A key factor was a favorable atmospheric circulation, marked by strengthened high-latitude systems and weaker mid-latitude systems (Chen and Dai, 2009). Combined with vertical circulation restructuring, enhanced moisture transport, and amplified atmospheric instability, these changes lead to extreme precipitation (Lu et al., 2021). Since the 1980s, phase shifts of oceanic oscillations have reorganized moisture transport pathways. A positive Atlantic Multidecadal Oscillation (AMO) together with Indian Ocean warming has weakened the East Asian Monsoon, while a negative Pacific Decadal Oscillation (PDO) has shifted the westerly jet poleward. These combined forcings established anomalous easterlies that effectively transport moisture from the North Pacific and high-latitude regions into NWC (Wang et al., 2014; Zhu et al., 2015; Qin et al., 2018; Chen et al., 2021a; Wu et al., 2022; Xue et al., 2022). Teleconnection patterns such as the East Asia/Pacific (EAP) wave train pattern and Silk-Road pattern (SRP) further modulated precipitation (Chen and Huang, 2012; Gong et al., 2018; Ning et al., 2021). The pronounced SRP phase shifts in the late 1970s and 1990s, which led to cyclonic anomalies over Central Asia and anticyclonic anomalies over Mongolia, enhanced ascent and instability, strengthened easterlies along the northern Tibetan Plateau, and a significant increase in moisture content (Xue et al., 2022). Since the 2000s, decadal adjustments of Eurasian wave trains have intensified downstream impacts through linkages among the North Atlantic Oscillation (NAO), Ural blocking, and East Asia, thereby modulating low-level convergence and moisture influx into NWC (Li et al., 2020; Shi et al., 2025).

Recent pronounced warming and humidification in NWC, marked by higher temperatures, greater precipitation, expanded vegetation, and stronger evapotranspiration, have greatly increased the hydrological complexity of the region. However, the sources and persistence of the moisture transport pathways that sustain humidification remain a matter of debate (Zhang et al., 2021). Although local evapotranspiration has increased, its specific contribution remains unquantified, and comparisons of local recycling versus external sources are limited. This study investigates the causes of increased precipitation in NWC by quantifying the contributions of moisture sources to precipitation and assessing circulation controls on precipitation using circulation diagnostics and moisture-budget calculations. The remainder of this paper is structured as follows. Section 2 details the datasets and methodology. Section 3 presents the findings: section 3.1 assesses spatiotemporal precipitation patterns; section 3.2 analyzes moisture transport variations; section 3.3 examines circulation anomalies associated with precipitation changes. Finally, section 4 discusses implications and presents conclusions.

2. Data and methodology

2.1. *Data*

The monthly precipitation data were obtained from Climate Research Unit Time-Series (CRU TS) version 4.06, covering the period from 1961 to 2020 at a spatial resolution of $0.5° \times 0.5°$ (Harris et al., 2020). To ensure data reliability in the study region, previous evaluations have indicated that the multi-year average precipitation of CRU shows good agreement with station observations in NWC (Wang et al., 2024). Meanwhile, the datasets of the Japanese 55-year Reanalysis project (JRA-55, Kobayashi et al., 2015) were also applied in this study, with a spatial resolution of $1.25° \times 1.25°$ and a temporal resolution of four times per day (0000 UTC, 0600 UTC, 1200 UTC, and 1800 UTC). The AMO index, with an estimated period of 60–80 years, is based on the average anomalies of sea surface temperatures (SST) in the North Atlantic basin, typically over 0°–80°N (Trenberth and Shea, 2006).

2.2. *Dynamic recycling model*

The Dynamic Recycling Model (DRM), which quantifies the contribution of local water vapor to regional precipitation, was applied to identify the moisture sources and estimate the precipitation recycling ratio (Dominguez et al., 2006, 2020). Derived from the atmospheric water vapor conservation equation, the DRM is a two-dimensional analytical model that accounts for moisture storage and assumes a well-mixed atmosphere (Dominguez et al., 2006). Unlike most simpler recycling models that neglect atmospheric water content changes (Brubaker et al., 1993; Schär et al., 1999), the DRM can be applied at daily temporal scales, allowing for more detailed estimation of precipitation recycling (Dominguez et al., 2006; Zhong et al., 2022). By tracking moisture budgets along transport trajectories, the model quantifies contributions from different source regions (Hua et al., 2017). The DRM has been widely employed in studies of the hydrological cycle across diverse regions worldwide, which supports its applicability in different climatic settings (Zhong et al., 2018; Herrera-Estrada et al., 2019). Considering that NWC is mainly situated within the westerlies with weak wind shear in terms of climatology, the DRM model is suitable for tracing moisture sources in this region (Ren et al., 2022; Zhang et al., 2022a).

2.3. *Moisture budget*

To diagnose the physical processes driving precipitation (P) changes, we conducted a moisture budget diagnostic analysis based on the atmospheric water budget equation (Seager and Vecchi, 2010; Seager et al., 2010, 2012; Chou and Lan, 2012). If we denote δ to indicate the difference between the periods of 1998–2020 (Period 2) and 1961–97 (Period 1, P1), the P anomalies (δP) can be decomposed as:

$$\delta P = -\delta\langle \mathbf{V}_{\mathrm{h}} \cdot \nabla_{\mathrm{h}} q\rangle - \delta\left\langle \omega \partial_{\mathrm{p}} q\right\rangle + \delta E + \mathrm{Res}\,, \qquad (1)$$

where q, $\mathbf{V}_{\mathrm{h}}$, ω and E denote the specific humidity, horizontal wind vector, vertical velocity, and evapotranspiration, respectively. The symbol $\langle\rangle$ denotes the mass vertical integration through the entire atmosphere. Res denotes the residual term primarily associated with transient eddies. Neglecting the sub-monthly transient eddies, the changes in vertical moisture advection $\left(\left\langle \omega \partial_{\mathrm{p}} q\right\rangle\right)$ and horizontal moisture advection ($\langle \mathbf{V}_{\mathrm{h}} \cdot \nabla_{\mathrm{h}} q\rangle$) can be further divided into three terms:

$$-\delta\left\langle \omega \partial_{\mathrm{p}} q\right\rangle = -\left\langle \overline{\omega_{\mathrm{P1}}} \partial_{\mathrm{p}} \delta \overline{q}\right\rangle - \left\langle \delta \overline{\omega} \partial_{\mathrm{p}} \overline{q_{\mathrm{P1}}}\right\rangle - \left\langle \delta \overline{\omega} \partial_{\mathrm{p}} \overline{q}\right\rangle\,, \qquad (2)$$

$$-\delta\langle \mathbf{V}_{\mathrm{h}} \cdot \nabla_{\mathrm{h}} q\rangle = -\left\langle \overline{\mathbf{V}_{\mathrm{h-P1}}} \cdot \nabla \delta \overline{q}\right\rangle - \left\langle \delta \overline{\mathbf{V}_{\mathrm{h}}} \cdot \nabla \overline{q_{\mathrm{P1}}}\right\rangle - \left\langle \delta \overline{\mathbf{V}_{\mathrm{h}}} \cdot \nabla \delta \overline{q}\right\rangle\,, \qquad (3)$$

where the overbars $\overline{(\cdot)}$ indicate the monthly mean flow. The first term on the right side in Eq. (2) and Eq. (3) represents the thermodynamic component (δTH) induced by specific humidity anomalies. The second term denotes the dynamic component (δMCD) induced by horizontal/vertical wind anomalies. The last term is defined as the nonlinear component (δNL) induced by specific humidity anomalies and horizontal/vertical wind anomalies.

2.4. *Linearized vorticity equation*

The vorticity budget analysis, based on the linearized vorticity equation, was used to explain the sustenance mechanism of enhanced precipitation. According to Kosaka and Nakamura (2006), under the geostrophic approximation, the linearized vorticity equation can be expressed as follows:

$$\mathrm{RWS} \underbrace{-\overline{u_{\varphi}}\frac{\partial \xi'}{\partial x}}_{\mathrm{ZA}} \underbrace{-\overline{v_{\varphi}}\frac{\partial \xi'}{\partial y}}_{\mathrm{MA}} \underbrace{-u'_{\varphi}\frac{\partial \overline{\xi}}{\partial x}}_{\beta\_x} \underbrace{-v'_{\varphi}\frac{\partial (f+\xi)}{\partial y}}_{\beta\_y} - \mathrm{RES} = 0\,, \qquad (4)$$

where RWS represents the linearized positive pressure Rossby wave source (Sardeshmukh and Hoskins, 1988), which can be divided into vorticity stretching and vorticity advection as follows:

$$\mathrm{RWS} = \underbrace{-\nabla_{\mathbf{H}}\left\{\boldsymbol{u}'_{\chi}\left(f+\overline{\xi}\right)\right\}}_{\textit{vorticity stretching}} \underbrace{-\nabla_{\mathbf{H}}\left\{\overline{\boldsymbol{u}_{\chi}}\xi'\right\}}_{\textit{vorticity advection}}\,, \qquad (5)$$

where $\nabla_{\mathbf{H}}$ represents the horizontal gradient operator, and $\boldsymbol{u} = (u, v)$ represents the horizontal wind. The subscripts φ and χ represent the rotational and divergent wind components of $\boldsymbol{u}$, respectively, ξ represents the relative vorticity, and f is the Coriolis parameter. ZA/MA represents the transport of disturbance vorticity by the zonal/meridional component of the rotating wind in climatological mean states, respectively. β_x/β_y represents the transport of mean vorticity by the disturbed zonal/meridional rotating wind, respectively. RES is the residual term, including the dissipation, nonlinear effect, skew term, and data uncertainty.

2.5. *The linear baroclinic model (LBM)*

The Linear Baroclinic Model (LBM; Watanabe and Kimoto, 2000) is a purely atmospheric diagnostic model developed to simulate atmospheric dynamical responses to idealized forcings such as diabatic heating. In our experiments, we employed the T42L20 version of LBM featuring T42 horizontal resolution and 20 vertical sigma levels. To ensure a stable response to heating forcings, the model was integrated over a period of 50 days, with the first 10 days serving as a spin-up phase. The response of the atmospheric circulation to diabatic heating was analyzed by averaging variables such as the meridional wind and geopotential height from day 20 to day 50.

3. Results

3.1. *The spatiotemporal variation of precipitation in Northwest China*

The spatial distribution of precipitation in NWC shows a margin-to-center decrease (Fig. 1a), with the highest summer precipitation amounts exceeding 250 mm in the northeastern, southeastern, and Tianshan Mountains. Further analysis of monthly precipitation and its contribution revealed that summer was the dominant rainy season (Fig. 1b), contributing 51.28% to the annual total. Specifically, the average monthly precipitation in June, July, and August was 30.95 mm, 40.39 mm, and 34.23 mm, respectively. The summer water vapor transport of NWC was driven by two primary pathways (Fig. 1c). The summer monsoon transported water vapor from mid-latitude regions into NWC, with a transport intensity of approximately 9×10^4 kg m^{-1} s^{-1}, and water vapor was also transported from the northwestern Eurasian continent, with an intensity of approximately 12×10^4 kg m^{-1} s^{-1}. Analysis of precipitation sources (Fig. 1d) identified local evapotranspiration in NWC, as well as moisture transport from northern Eurasian (NEA), central and midwestern Eurasia (WCEA), Eastern China (EC), and the Indian Subcontinent and Northern Indian Ocean (ISNIO) as primary sources. Among these, local evapotranspiration in NWC made the greatest contribution, accounting for 44.50%, followed by that in NEA (26.96%) and WCEA (8.14%). In contrast, the contributions from EC (4.72%) and ISNIO (3.25%) were minor, while the North Atlantic Ocean (NAL, 0.82%), North Africa and West Asia (NAFWA, 0.19%), and South Indian Ocean (SIO, 0.17%) were negligible. Overall, the summer precipitation in NWC primarily depends on external moisture transport in terms of climatology.

After gaining an initial understanding of the climatic summer precipitation characteristics in NWC, we further investigated the precipitation trends from 1961 to 2020. The spatial distribution of the summer precipitation trend (Fig. 2a) indicated a clear increase over the Tianshan and Altun Mountains. However, the central Taklamakan Desert, Lake Balkhash, and northeastern drylands experienced significant declines, forming a distinct east–west contrast, which was characterized by increased precipitation in the west and decreased precipitation in the northeast. An Empirical Orthogonal Function (EOF) analysis of annual precipitation further clarified this pattern. The first principal mode (EOF1) showed near-uniform interannual variability with no significant long-term trend or interdecadal shift, contributing little to regional humidification. In contrast, the second principal mode (EOF2) showed an east-west contrast (Fig. 2b), explaining 15.6% of the variance. Its time coefficient (PC2) exhibited pronounced interdecadal variability: the cumulative

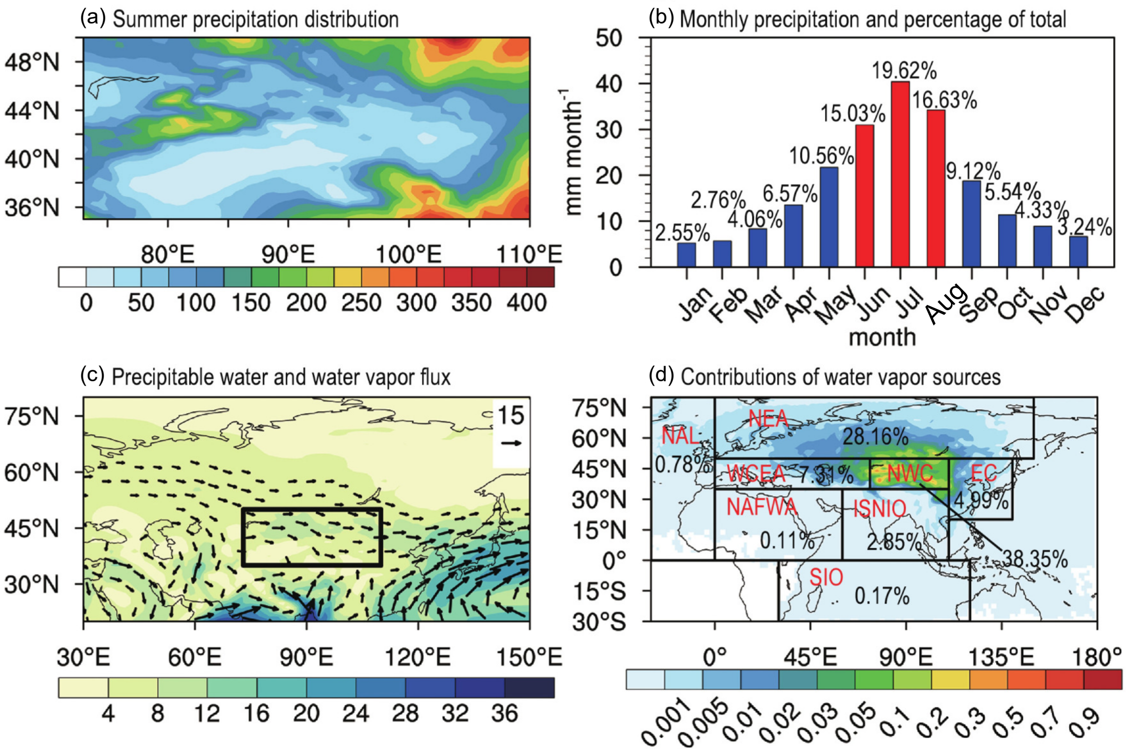

Fig. 1. (a) Spatial distribution of summer precipitation in NWC from 1961 to 2020 (units: mm). (b) Monthly precipitation and the percentage relative to annual precipitation from 1961 to 2020 (units: mm month^{-1}). (c) Spatial distribution of precipitable water (shaded, units: 10^4 kg m^{-1} s^{-1}) and vertical integrated water vapor flux (vector, units: 10^4 kg m^{-1} s^{-1}) during summer from 1961 to 2020. The black box in (c) indicates the location of NWC. (d) Spatial distribution of contributions from different water vapor sources to summer precipitation in NWC (units: %). The black boxes in (d) represent the defined geographic regions: NWC (73°–110°E, 35°–50°N), NAL (30W°–0°, 0°–80°N), NEA (0°–150°E, 50°–80°N), WCEA (0°–73°E, 35°–50°N), NAFWA (0°–25°E, 35°–50°N), ISNIO (60°–110°E, 0°–35°N), SIO (30°–120°E, 30°S–0°), and EC (110°–140°E, 20°–50°N).

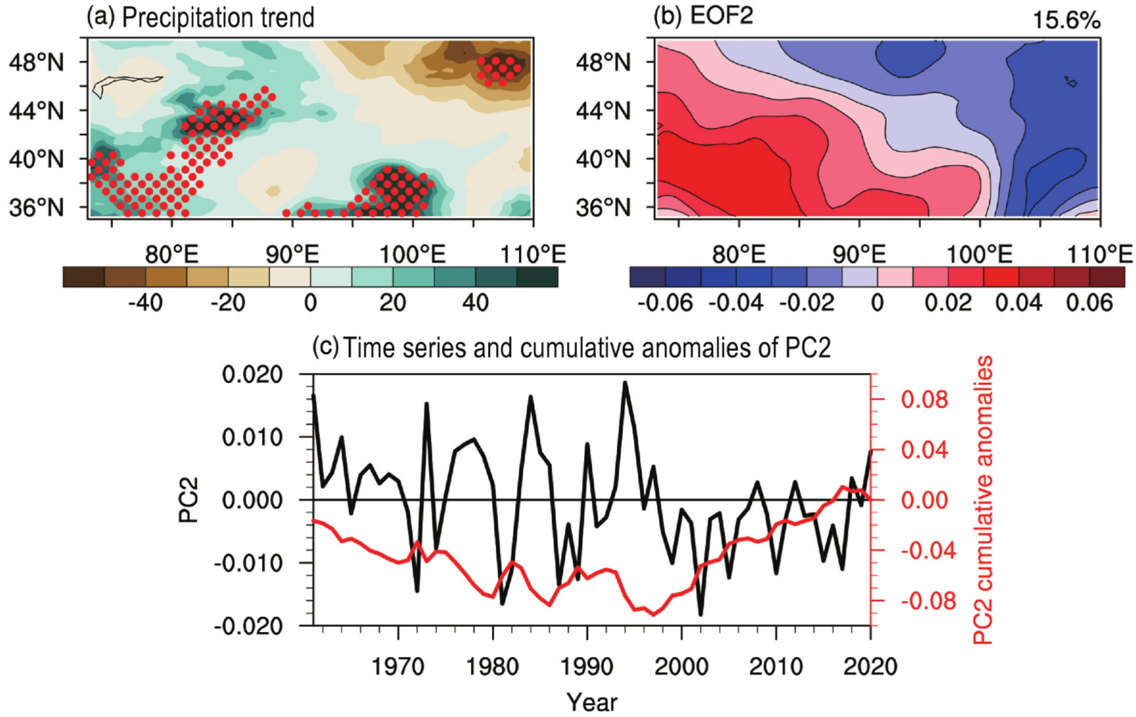

Fig. 2. (a) Spatial distribution of the summer precipitation trends in NWC from 1961 to 2020 (units: mm yr^{-1}). The red dots indicate that the changes are significant at the 95% level. (b) The second leading EOF mode pattern of summer precipitation in NWC from 1961 to 2020. (c) The time series (black line) and cumulative anomalies (red line) of PC2.

anomaly declines before 1997 and rises thereafter (Fig. 2c). To clarify the mechanisms underlying this interdecadal shift, we compared surface water balance conditions between the 1961–97 and 1998–2020 means.

3.2. *Moisture sources for increased precipitation*

To further investigate the water vapor sources of the humidification trend in NWC, we applied the DRM model to separate source contributions. The precipitation produced by the internal cycle is defined as recycled precipitation, and the precipitation that originated from moisture that was brought into the region by advection is defined as advected precipitation (Lettau et al., 1979; Burde et al., 1996; Dominguez et al., 2006). Summer precipitation changes (Fig. 3a) exhibited a distinct west-east contrast, consistent with the spatial pattern of trends presented in Fig. 2a. Specifically, precipitation significantly increased by approximately 10 mm over western regions, especially in the Tianshan and Altun Mountains (Figs. 3a, b). Concurrently, enhanced evapotranspiration (Fig. 3d) elevated recycling rates (Fig. 3e), and the spatial coherence between intensified recycled precipitation and observed humidification identifies the increased local evapotranspiration as the leading moisture source. In contrast, northeastern areas experienced precipitation decreases of up to 30 mm (Fig. 3a). The decline was mainly due to a reduction in advected moisture (Fig. 3c). Specifically, reductions in advected precipitation (approximately 4–8 mm) exceeded decreases in recycled precipitation (approximately 0–4 mm).

To clarify the moisture transport responsible for humidification in NWC, we quantified boundary moisture fluxes as well as local evapotranspiration, and analyzed circulation changes for the humidification (Fig. 4f). Compared to 1961–97, precipitable water during 1998–2020 exhibited significant positive anomalies over most areas. Among the boundaries, the western boundary (Fig. 4d) supplied the largest mean inflow [approximately (1–4) × 10^9 kg s^{-1}]. Moisture flux across the southern boundary (Fig. 4e) increased significantly and reversed from net export to import after the late 1990s, driven by a cyclone that advected Arabian Sea moisture northeastward. The northern boundary (Fig. 4b) imported moisture at a relatively small magnitude with no significant trend. As the primary export pathway, the eastern boundary experienced a marked decline in outflow (Fig. 4c) under anticyclone-driven easterlies, thereby suppressing regional moisture loss. Enhanced evapotranspiration served as a major internal moisture source (Fig. 4a). Mean evapotranspiration [(2.0–2.8) × 10^8 kg s^{-1}] significantly increased after 1997, consistent with positive evapotranspiration anomalies shown in Fig. 3e. Superimposed anomalies in atmospheric circulation, notably the intensified Mongolian Plateau anticyclone and a weakened Indian summer monsoon, further modulated boundary fluxes and reinforced regional moistening.

From 1961 to 2020, the total precipitation increase in NWC was 22.15±1.28 mm, of which 17.39±0.73 mm came from recycled precipitation and 3.79±0.66 mm from advected precipitation. In comparing the 1961–97 and

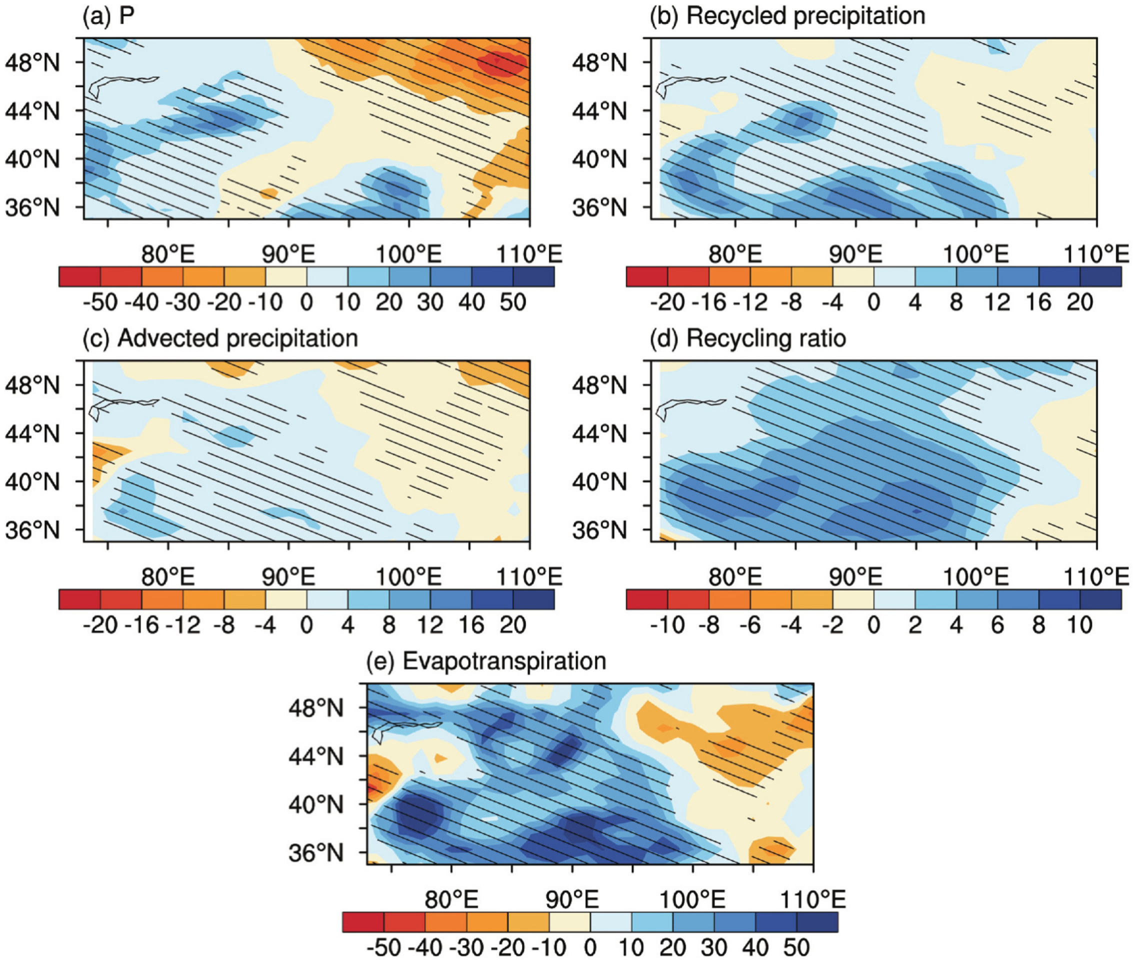

Fig. 3. Spatial patterns of differences between the 1961–97 mean and 1998–2020 mean for (a) precipitation (units: mm), (b) recycled precipitation (units: mm), (c) advected precipitation (units: mm), (d) recycling ratio (units: %), and (e) evapotranspiration (units: mm). The black-shaded slash indicates differences that are significant at the 95% level.

1998–2020 mean values, the contribution of moisture from local evapotranspiration within NWC increased by 3.08%, while that from NEA decreased by 3.77%, whereas the contribution of WCEA decreased by 0.98%; thus local evapotranspiration was the most significant driver of moisture changes in NWC (Fig. 5a). This finding indicates that the recent increase in precipitation was primarily driven by enhanced local moisture recycling, consistent with the results shown in Fig. 3. As shown in Fig. 5b, there was a notable shift in both the total precipitation and the related water vapor sources between the 1961–97 and 1998–2020 periods. In 1961–97, total precipitation averaged 122.59 mm yr^{-1}, with recycled precipitation accounting for 41.02% and advected precipitation contributing 51.97%. However, in the 1998–2020 period, the total precipitation rose to 133.21 mm yr^{-1}, within which, the recycled precipitation contribution increased to 45.13%, while the advected precipitation contribution decreased to 48.08%. A comparative moisture budget analysis (Fig. 5c) revealed that despite a decrease in vapor inflow (F_{in}), a concurrent reduction in outflow (F_{out}) led to a net increase in precipitable water over NWC (Fig. 4). Consequently, precipitation from external vapor advection (P_a) increased by 8.45%. This was compounded by a 10.51% rise in recycled precipitation (P_e), which collectively drove a 9.18% increase in total precipitation (P). This shift was primarily attributable to a 9.12% enhancement in evapotranspiration (E). Despite the climatological dominance of external vapor transport, the interdecadal increase of precipitation in NWC has been principally caused by local evapotranspiration, due to its more rapid acceleration compared to the net moisture inflow.

To clarify how humidification reshaped the water cycle, we decomposed Eq. (3) described in section 2.3 to attribute the interdecadal change in P to individual moisture budget terms (Fig. 5d). In summer, both P and E exhibited positive anomalies of 10.62 mm yr^{-1} and 10.32 mm yr^{-1}, respectively. Specifically, the vertical water vapor component (ver) added +1.33 mm yr^{-1} to P, which was primarily driven by the vertical thermodynamic term (ver_TH, +1.68 mm yr^{-1}), with smaller contributions from the horizontal thermodynamical term (hor_TH, +0.80 mm yr^{-1}) and vertical nonlinear term (ver_NL, +0.87 mm yr^{-1}). Conversely, the horizontal dynamical term (hor_MCD) and nonlinear term (hor_NL) yielded respective

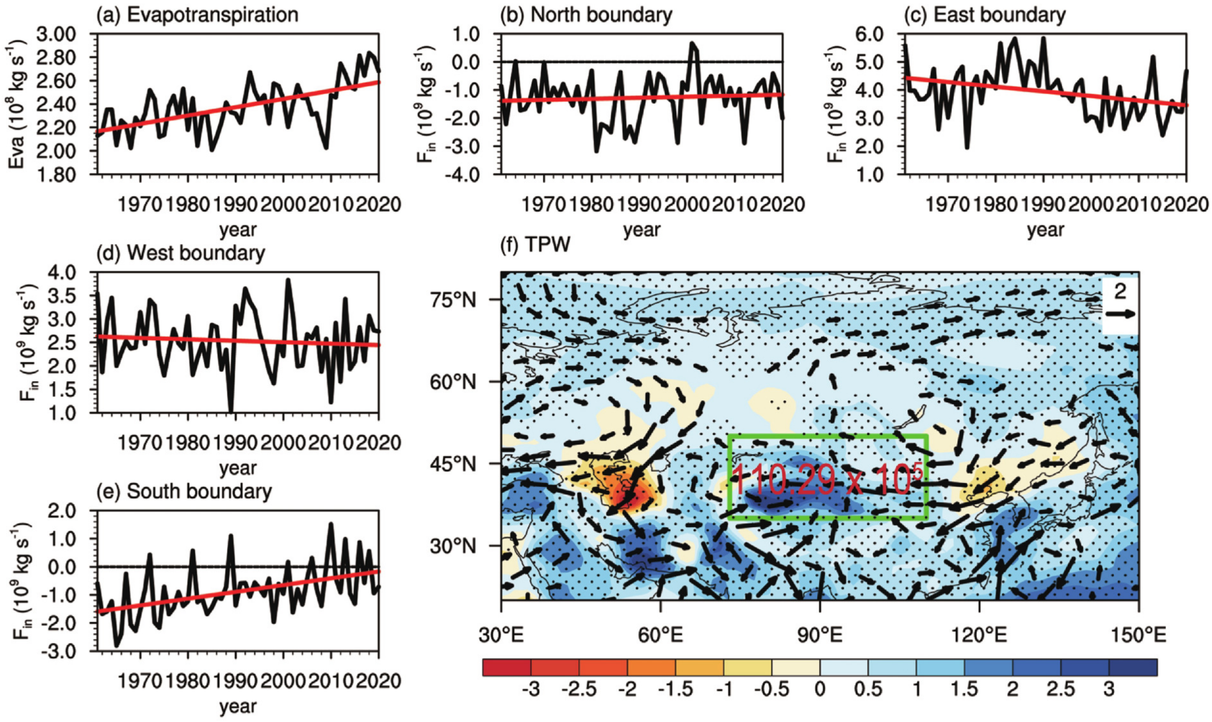

Fig. 4. Yearly variations of the evapotranspiration and water vapor budget at the boundaries and their trends of NWC in summer from 1961 to 2020: (a) evapotranspiration (units: 10^8 kg s^{-1}); (b) north boundary (units: 10^9 kg s^{-1}); (c) east boundary (units: 10^9 kg s^{-1}); (d) west boundary (units: 10^9 kg s^{-1}); (e) south boundary (units: 10^9 kg s^{-1}). The black lines represent temporal variations, and the red lines represent the corresponding linear trends. (f) Spatial patterns of differences between the 1961–97 mean and 1998–2020 mean for precipitable water (shaded, units: 10 kg m^{-1} s^{-1}) and vertical integrated water vapor flux (vector, units: 10 kg m^{-1} s^{-1}) in summer. The black dots indicate changes that are significant at the 95% level.

reductions of −1.01 and −0.89 mm $year^{-1}$, so the net horizontal component (hor) contribution was small (−1.11 mm $year^{-1}$). Because the nonlinear effects were minor (Fig. 5d), the subsequent analysis focuses primarily on the dynamical and thermodynamical controls affecting *P* changes.

In the analysis of horizontal components, we used the 700-hPa wind field and specific humidity for circulation analysis. The horizontal thermodynamic term reflects a synergistic enhancement between changes in humidity gradients and wind fields (Fig. 6b). The prevailing westerlies at 700 hPa aligned with a pattern of humidity increase that strengthened to the north (Fig. 6d). This coupling effectively extended moisture advection northward and augmented local transport and storage, resulting in a positive thermodynamic anomaly (Fig. 6b). In contrast, the horizontal dynamical term indicated a mismatch between the wind vectors and the specific-humidity gradient. These opposing vectors suppressed net moisture influx, leading to a negative dynamical contribution (Figs. 6a, c). Therefore, although vertical thermodynamic and horizontal thermodynamic processes jointly enhanced precipitation, horizontal dynamical adjustments partially offset regional moistening.

In the analysis of vertical water vapor advection, we follow the method of Jin et al. (2020) and approximate the full term as the product of 500-hPa vertical velocity (ω_{500}) and 700-hPa specific humidity (q_{700}). Specifically, we approximated the troposphere using a two-layer model, with the interface at 500 hPa. We assumed that the average specific humidity (q) in the lower troposphere is equal to the q_{700}, while the specific humidity in the upper troposphere is negligible. Based on these assumptions, the following approximation is derived:

$$\left\langle \omega \partial_{\mathrm{p}} q \right\rangle \approx \frac{1}{\mathrm{g}} (\omega_{500} q_{700}) \, , \tag{6}$$

$$\langle \mathbf{V}_{\mathrm{h}} \cdot \nabla_{\mathrm{h}} q \rangle \approx \frac{1}{\mathrm{g}} (\mathbf{V}_{700} \cdot \nabla q_{700}) \, . \tag{7}$$

The vertical dynamic term ($\delta\overline{\omega}\partial_{\mathrm{p}}\overline{q_{\mathrm{P1}}}$) is represented as the product of the interdecadal difference in ω_{500} and the 1961–97 climate average of q_{700}, while the horizontal dynamic term ($\delta\overline{\mathbf{V}_{\mathrm{h}}}\nabla\overline{q_{\mathrm{P1}}}$) is the product of the interdecadal difference in V_{700} and the 1961–97 climate average of q_{700}. By examining the distribution of these variables, we can visually illustrate the impact of circulation changes on precipitation variability. This approach relies on two assumptions: (1) the water vapor is mainly concentrated near 700 hPa in the troposphere; (2) the 500-hPa level is key for vertical motion. With these assumptions, the vertical and horizontal water vapor transport terms are simplified: the vertical trans-

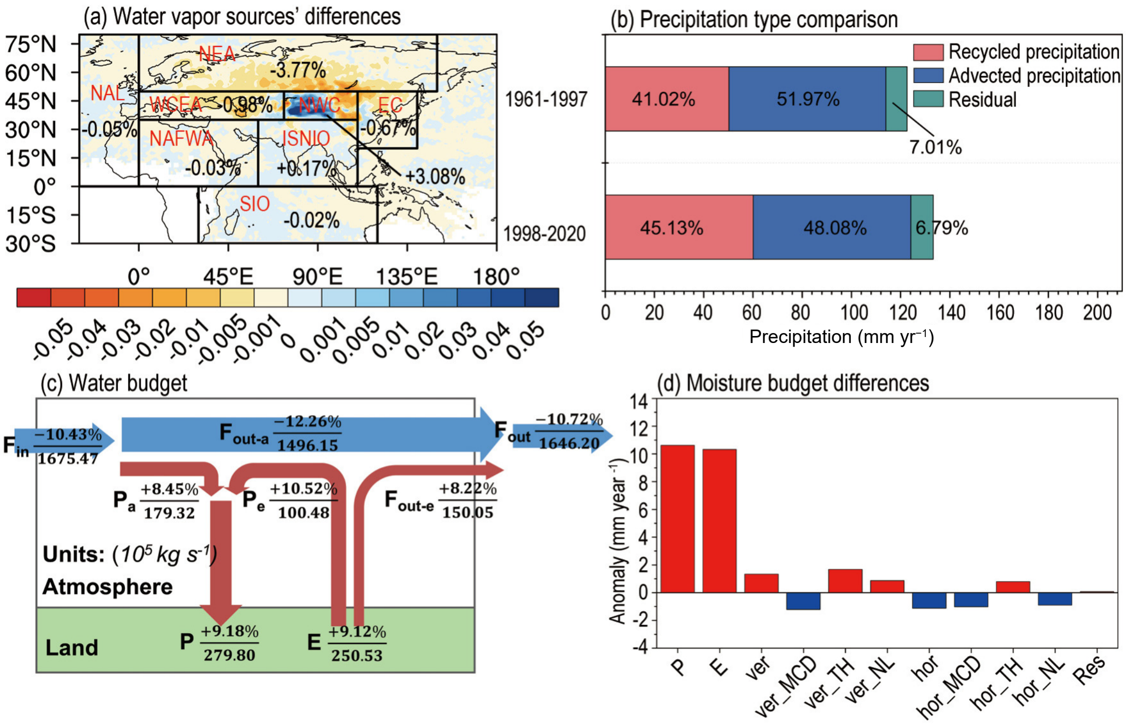

Fig. 5. (a) Spatial patterns of differences between the 1961–97 mean and 1998–2020 mean for contributions from different water vapor sources to summer precipitation in NWC (units: %). (b) Comparison of summer precipitation types in NWC between the 1961–97 mean and 1998–2020 mean (the unit is mm yr^{-1} for precipitation and % for contribution). (c) The 1998–2020 mean for various variables in summer (units: 10^5 kg s^{-1}), with the numerator representing the differences between the 1961–97 mean and 1998–2020 mean. $F_{out\text{-}a}$ and $F_{out\text{-}e}$ represent the outflowing water vapor produced by the horizontal moisture and local evapotranspiration, respectively. (d) Differences between 1961–97 mean and 1998–2020 mean for summer moisture budget in NWC (units: mm yr^{-1}). The "Ver" and "Hor" represent the vertical and horizontal water vapor advection terms, which represent the sum of their respective MCD, TH, and NL terms.

port is primarily governed by the 500-hPa vertical velocity and 700-hPa specific humidity, while the horizontal transport is controlled by the 700-hPa horizontal wind field and specific humidity gradients. This two-layer approximation captures the essential physics of moisture transport. Under positive specific humidity anomalies, vertical motion weakened significantly across most of NWC, except for the Tianshan and Altun Mountains (Fig. 7c). The resulting covariance between humidity and vertical velocity produced a negative vertical dynamical contribution (Fig. 7a), which weakened the upward moisture transport. Spatially, the southwestern subregion showed strong ascent, whereas subsidence prevailed in the central area (Fig. 7d). This dipole pattern was clearly reproduced in the vertical thermodynamic contribution, which was positive in the southwest but negative over the central region (Figs. 7b, d). The close correspondence between these two fields confirmed that vertical velocity primarily drives the vertical thermodynamic term in the regional moisture budget.

3.3. *Circulation mechanisms driving increased precipitation*

Spatial patterns of the differences between the 1961–97 and 1998–2020 subsets revealed an eastward-propagating Rossby wave train propagating energy from the North Atlantic to Eurasia (Fig. 8a). At 500 hPa, a ridge dominated the western drylands of NWC, while a trough prevailed over the eastern section (Fig. 8b). In static equilibrium, the ridge was characterized by anomalous warming, whereas the trough corresponded to anomalous cooling (Fig. 8c). The associated vertical motion featured pronounced ascent over western NWC (upstream of the ridge) and compensating subsidence further east (Fig. 8d). This vertically coupled circulation, embedded within the trans-Eurasian wave train, regulated the opposing horizontal and vertical moisture transports, ultimately determining the spatial distribution of precipitation in NWC.

T-N wave activity diagnostics identified the North Atlantic as the source of eastward-propagating Rossby waves that modulated the interdecadal precipitation in NWC. These waves were excited by diabatic heating and transient eddy feedback. A comparison of the mean summer SSTs between 1998–2020 and 1961–97 (Fig. 9a) reveals a basin-wide warming, consistent with a positive AMO phase. The regression of the 1961–2020 AMO index onto the meridional winds and T-N fluxes at 250 hPa (Fig. 9b) shows a coherent wave train extending from the North Atlantic to

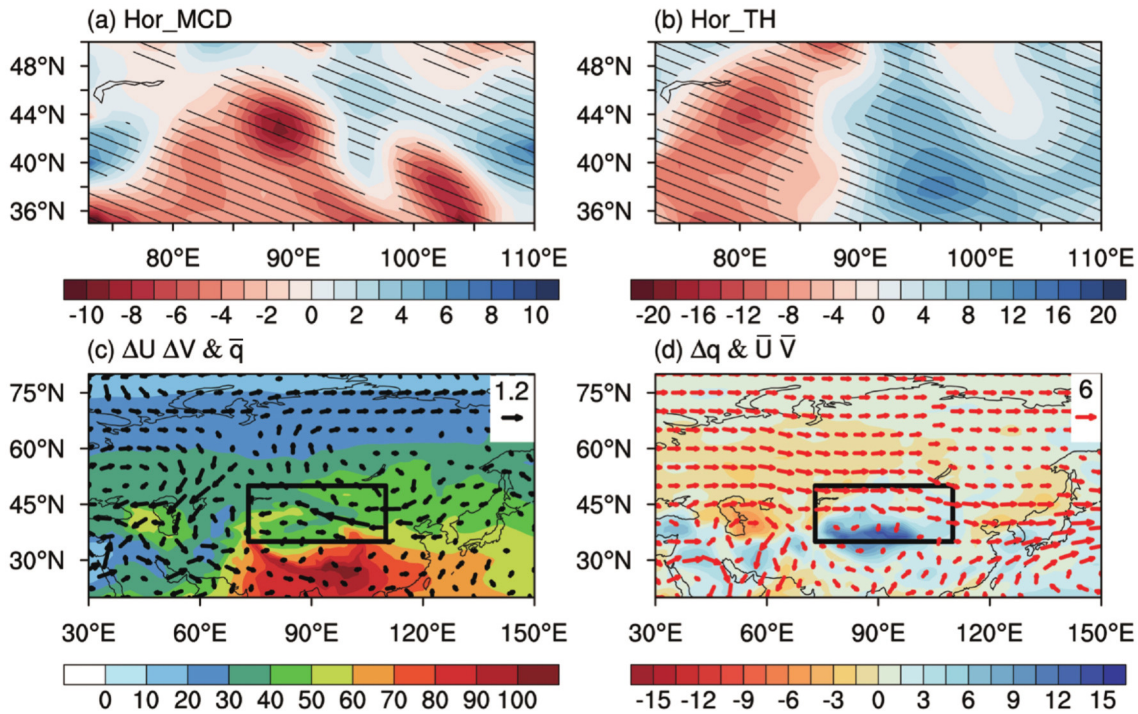

Fig. 6. Spatial distribution of the (a) horizontal dynamic and (b) thermodynamic components of summer precipitation (units: mm yr^{-1}). The black-shaded slash indicates differences that are significant at the 95% level. The corresponding wind changes (black vector; units: m s^{-1}) and the 1961–97 mean specific humidity at 700 hPa (shaded; units: 10^{-4} kg kg^{-1}) for the horizontal dynamic component are shown in (c). Changes in specific humidity (shaded; units: 10^{-4} kg kg^{-1}) and the 1961–97 mean wind at 700 hPa (red vector; units: m s^{-1}) for the horizontal thermodynamic component are presented in (d).

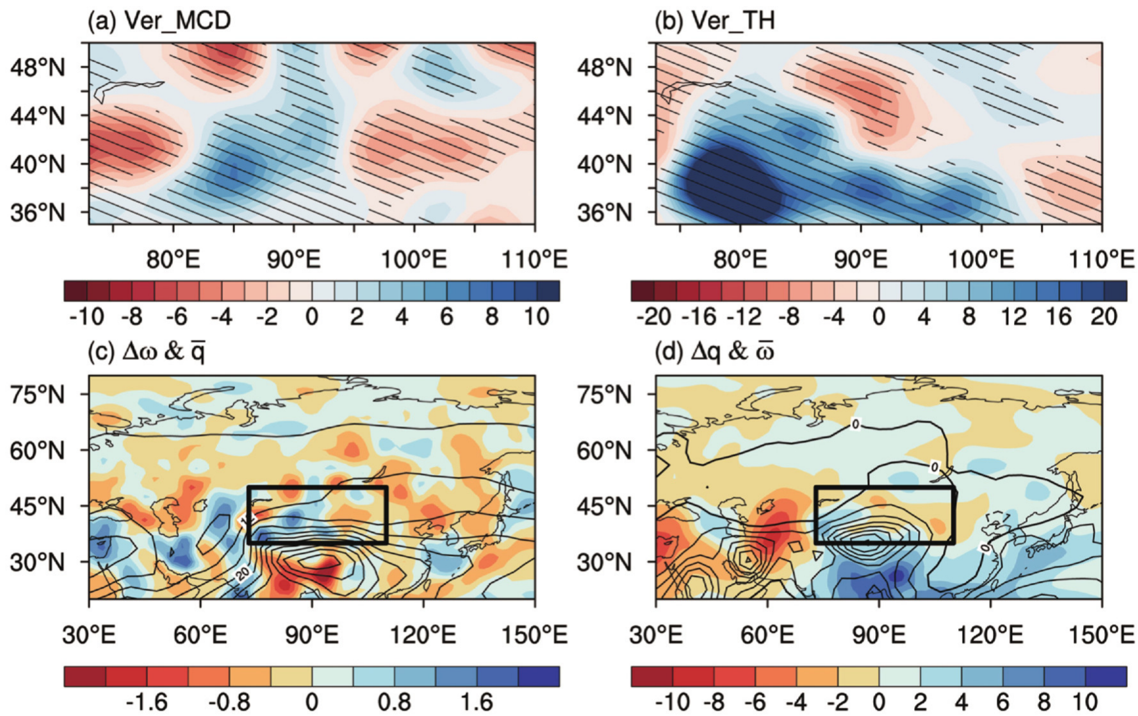

Fig. 7. Same as in Fig. 6, but for vertical (a) dynamic and (b) thermodynamic components (units: mm yr^{-1}). The black-shaded slash indicates differences that are significant at the 95% level. (c) Changes in the 500-hPa vertical velocity (shaded; units: –1 Pa s^{-1}) and the 1961–97 mean 700-hPa specific humidity (black lines; units: 10^{-5} kg kg^{-1}) for the vertical dynamic component. (d) Changes in the 700-hPa specific humidity (black lines; units: 10^{-5} kg kg^{-1}) and the 1961–97 mean 500-hPa vertical velocity (shaded; units: 1 Pa s^{-1}) for the vertical thermodynamic component.

East Asia, which closely matched the anomaly pattern in Fig. 8a. The corresponding height and wind regressions at 500 hPa (Fig. 9c) showed that the geopotential height anomalies aligned with the upper-level wind centers, confirming a barotropic circulation pattern associated with the AMO, similar to that in Fig. 8b. A meridional cross-section along the wave guide (red line in Figs. 9b and 9d) revealed alternating ridges and troughs throughout the troposphere, with temperature anomalies co-located with height anomalies, indicating strong meridional heat transport. Collectively, the results implicate an AMO-driven North Atlantic SST warming as the driver of a barotropic Rossby wave train that crosses Eurasia and reorganizes the mid-latitude circulation. Such a dependence suggests a potential unsustainability of the humidification in NWC under the prospect of future changes in the AMO phase.

The linear barotropic vorticity equation (Fig. 10) clarifies the origin and propagation of the trans-Eurasian wave train. The vorticity budget is primarily dominated by RWS, ZA, and β_y. The RWS field mirrored the stationary Rossby pattern (SRP), with alternating anticyclonic centers along the upper-level westerly jet (Figs. 8a, b) over the northern North Atlantic, central Europe, and East Asia, while cyclonic centers were positioned over western Europe and Central Asia. ZA (Fig. 10b) and β_y (Fig. 10e) were approximately an order of magnitude larger than the other terms, but opposed each other. This suggests that the mean-flow advection of perturbation vorticity was nearly offset by the β_y term, which is characteristic of a quasi-stationary Rossby wave along the jet stream. By comparison, MA (Fig. 10c) and β_x (Fig. 10d) were negligible. The decomposition of RWS into its stretching and advection components showed a clear dominance of the stretching term (Fig. 10g), suggesting that upper-tropospheric divergence and convergence anomalies served as the primary driver of wave source generation (Xu et al., 2019). Overall, the diagnostics suggest that an anomalous diabatic heat source over the North Atlantic triggered upper-level convergence and divergence, initiating the RWS. The resulting wave train was sustained by a balance between zonal advection and the β effect as it propagated eastward.

Figure 11 shows that the anomaly centers of all key variables are aligned in a coherent west-to-east tripolar pattern over Eurasia. Ascent in western NWC enhanced condensation and cloud formation, resulting in a positive total cloud anomaly (Fig. 11a). The increase in cloud cover strengthened the absorption and scattering of solar radiation, thereby reducing the surface downward shortwave flux (Fig. 11b). Surface cooling followed, narrowing the surface air-temperature gradient and weakening the upward longwave radiation (Fig. 11c) and sensible heat flux (Fig. 11d). At the same time, the cloud-rich regions enhanced more precipitation (Fig. 3a) and developed positive soil moisture anomalies (Fig. 11e). This moisture surplus enhanced local evapotranspiration and consequently increased the latent heat flux (Fig. 11f). In the eastern subsidence region, reduced cloudiness admitted more solar radiation to the surface (Fig. 11b). The ground warmed, and upward longwave radiation (Fig. 11c) and sensible heat flux increased (Fig. 11d). Meanwhile, negative soil moisture anomalies suppressed evapotranspiration, resulting in a negative latent heat flux anomaly (Fig. 11f). Thus, although precipitation variability was mainly governed by

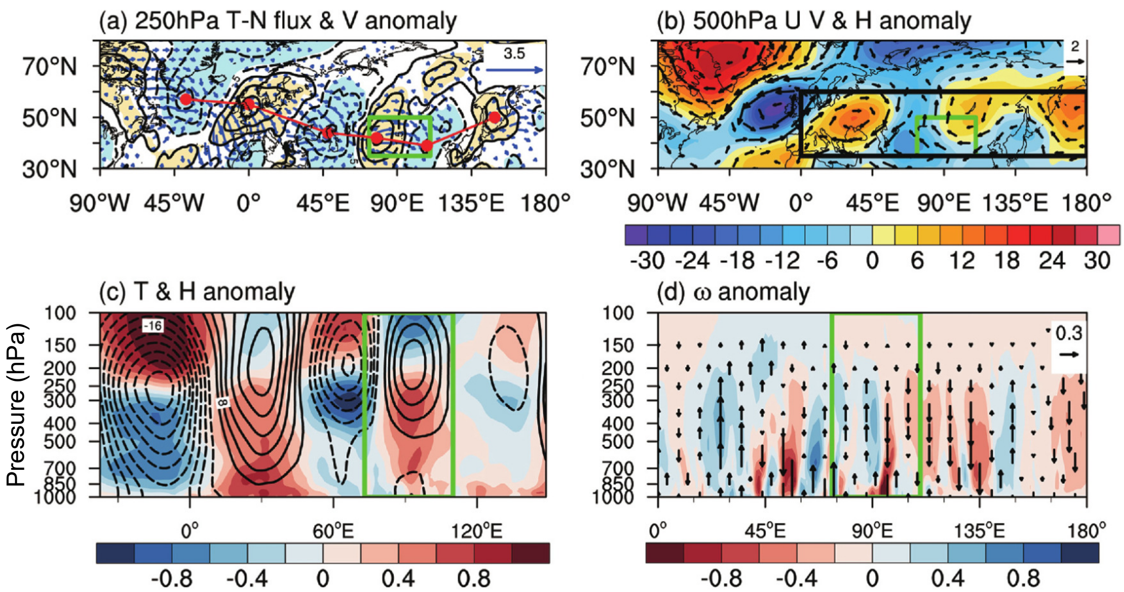

Fig. 8. Spatial patterns of differences between the 1961–97 mean and 1998–2020 mean for the (a) 250-hPa meridional wind (black lines; units: m s^{-1}) and T-N wave activity flux (vectors; units: m^2 s^{-2}); (b) geopotential height (shaded; units: gpm) and wind (black vectors; units: m s^{-1}) at 500 hPa; (c) vertical profile of the temperature (shaded; units: K) and geopotential height (black lines; units: gpm) along the red line in (a); (d) zonally averaged vertical profile of vertical velocity (units: m s^{-1}) along the black box in (b). The shaded areas in (a) indicate differences that are significant at the 95% level. The green box indicates the location of NWC.

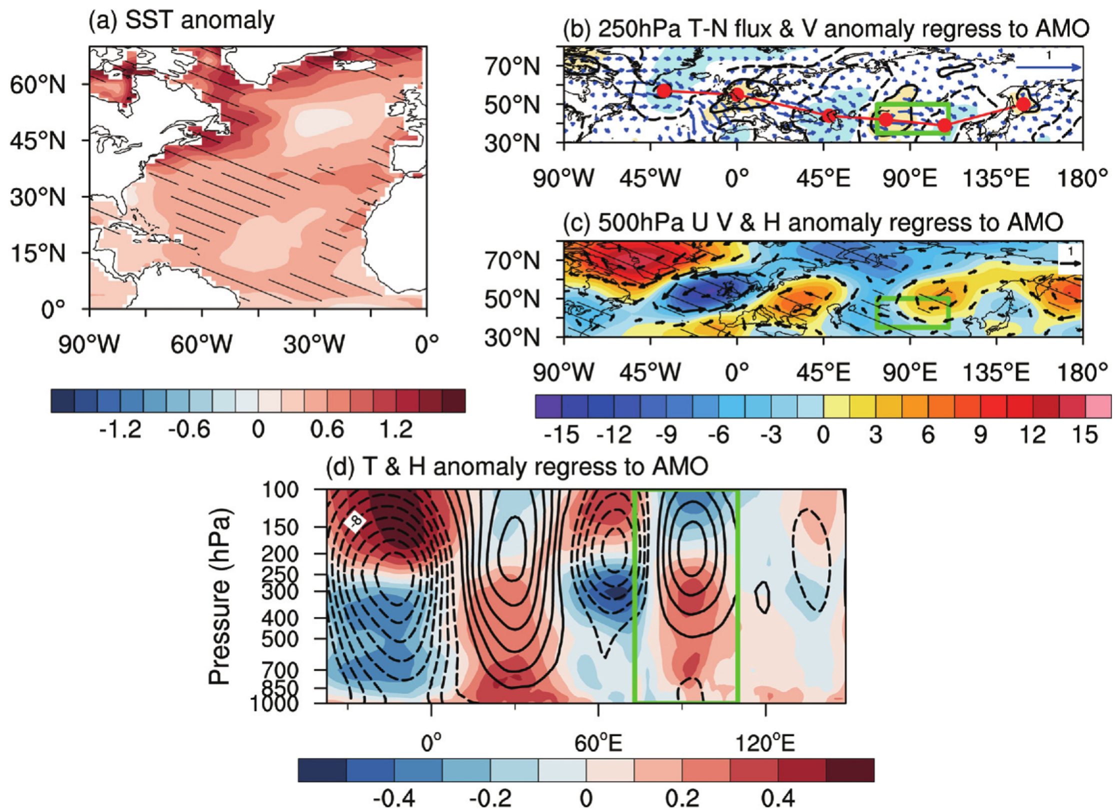

Fig. 9. (a) Spatial patterns of the differences between the 1961–1997 mean and 1998–2020 mean for the summer sea surface temperature (SST) of the North Atlantic. The black-shaded slash in (a) indicates differences that are significant at the 95% level. (b) 250-hPa meridional wind (black lines; units: m s^{-1}) and T-N wave activity flux (vectors; units: m^2 s^{-2}) regressed onto the AMO index during 1961–2020, with shaded areas indicating regressions that are significant at the 95% level. (c) 500-hPa geopotential height (shaded; units: gpm) and wind (black vectors; units: m s^{-1}) regressed onto the AMO index during 1961–2020. The black-shaded slash in (c) indicates differences whose regressions are significant at the 95% level. (d) Vertical profile of the temperature (shaded; units: K) and geopotential height (black lines; units: gpm) regressed onto the AMO index along the red line in (b). The green box indicates the location of NWC.

dynamically induced vertical motion, concurrent shifts in the surface energy balance highlighted the key role of evapotranspiration in regional moisture transport.

The summer vorticity anomalies at 500 hPa over the North Atlantic exhibited a dipole structure, characterized by a strong positive center at high latitudes and a negative center at mid-latitudes (Fig. 12a). Two key regions were identified: a positive core (Region 1; 47°–58°N, 12°–37°W; green box) and a negative core (Region 2; 32°–40°N, 12°–35°W; purple box). Vertical cross-sections through these regions (Fig. 12b) showed that the vorticity maxima peaked near 250 hPa. To evaluate whether these disturbances could initiate an eastward-propagating Rossby wave, we used a Linear Baroclinic Model (LBM), driven by the vertical vorticity profile shown in Fig. 12b, to analyze the atmospheric response. Between simulation days 20 and 50 (Fig. 12c), the 250 hPa meridional wind field exhibited alternating positive and negative anomalies, forming a coherent wave train from the North Atlantic to East Asia. A distinct dipole appeared over NWC, consistent with Fig. 8a. These LBM results confirmed that North Atlantic vorticity anomalies served as an effective source of eastward-propagating Rossby waves and modulated the interdecadal variability of precipitation in NWC.

4. Conclusion and discussion

This study analyzed the spatial patterns, trends, moisture sources, and physical mechanisms of summer precipitation in Northwest China during 1961–2020 (Fig. 13). The results reveal a clear contrasting pattern characterized by a western increase and an eastern decrease in precipitation trends across NWC, with a notable shift occurring around 1997. Although the main water vapor sources for precipitation in NWC under climatology were external moisture transport, the increase of precipitation after 1997 was dominated by local evapotranspiration. The interdecadal change of precipitation is modulated by the AMO through an eastward Rossby wave train across Eurasia, producing ridging with ascent and moisture convergence in the west and troughing with subsidence and divergence in the northeast. This circulation also reduced eastward moisture export from NWC, reinforcing local recycling. Overall, increased local evapotranspira-

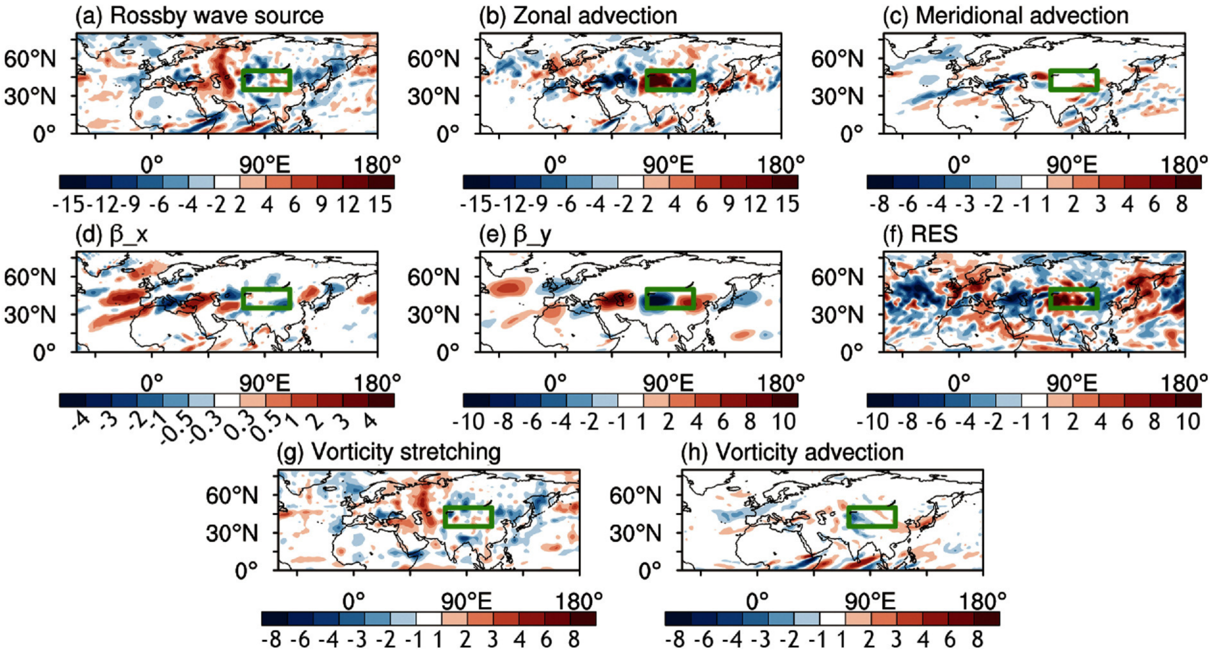

Fig. 10. Composite anomalies of the vorticity budget of 200-hPa winds in summer during 1961–2020: (a) the Rossby wave source term (RWS); (b) the zonal advection term (ZA); (c) the meridional advection term (MA); (d) the transport of mean vorticity by disturbed zonal rotating wind (β_x); (e) the transport of mean vorticity by disturbed meridional rotating wind (β_y); (f) the residuals (RES); (g) the vortex stretching term; (h) the absolute vorticity advection term. The green box indicates the location of NWC. Units: 10^{-11} s^{-1}.

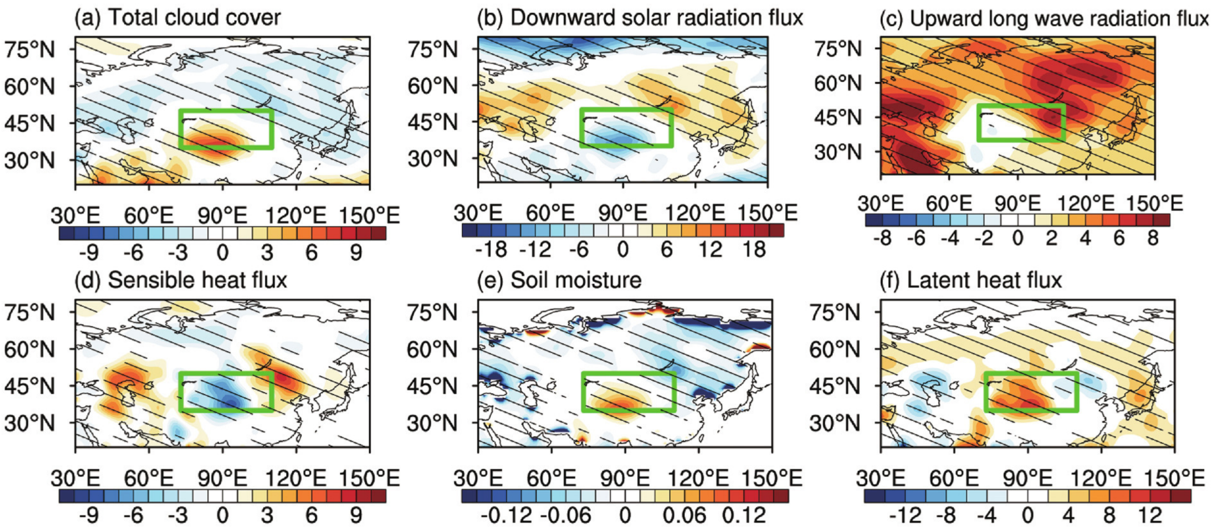

Fig. 11. Spatial patterns of differences between the 1961–97 mean and 1998–2020 mean for: (a) total cloud cover (units: %); (b) surface downward solar radiation flux (units: W m^{-2}); (c) upward longwave radiation flux (units: W m^{-2}); (d) surface sensible heat flux (units: W m^{-2}); (e) soil moisture (units: %); (f) surface latent heat flux (units: W m^{-2}). The black-shaded slash indicates differences that are significant at the 95% level. The green box indicates the location of NWC.

tion and weakened eastward export led to a net moisture increase and stronger post-1997 rainfall in NWC.

It is important to note that the DRM model used in this study is based on the assumption of a two-dimensional wind field for moisture trajectory tracking, which does not fully account for the vertical shear effects of the horizontal wind. Consequently, when upper-level and lower-level winds oppose each other, transport could differ from the vertically averaged 2-D wind, leading to different transport directions from local and distant sources (Van Der Ent and Savenije, 2013; Martinez and Dominguez, 2014). Moreover, the coarse resolution of the reanalysis data prevents full representation of steep topography, adding uncertainty to water vapor transport estimates. Future research should focus on

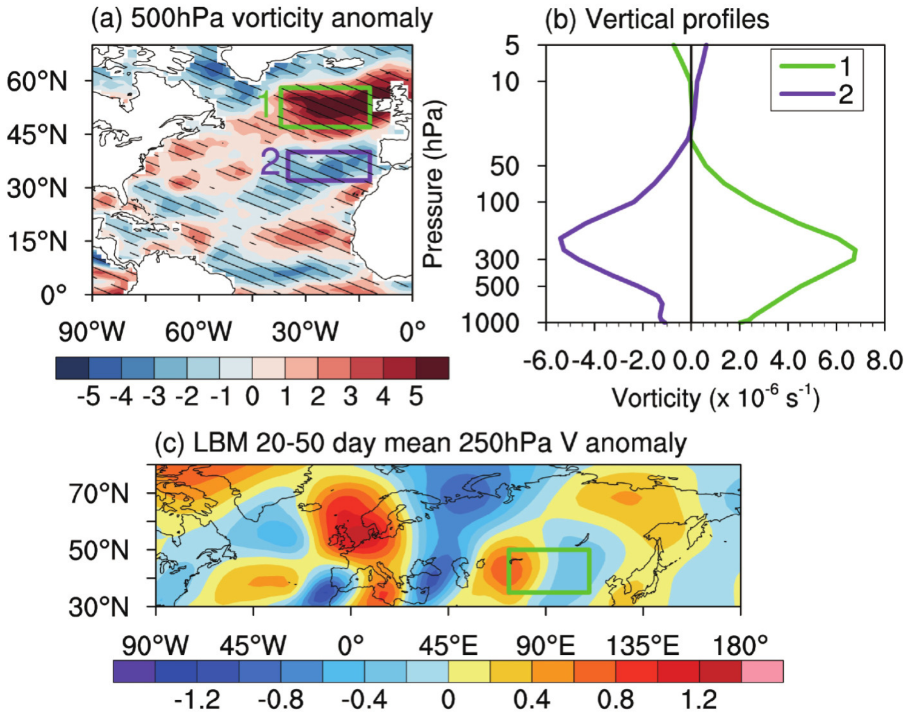

Fig. 12. Selection of the LBM vorticity sensitivity test. (a) Spatial patterns of differences between the 1961–97 mean and 1998–2020 mean for the 500-hPa vorticity in summer (units: 10^{-11} s^{-2}). The black-shaded slash indicates differences that are significant at the 95% level, and the two significant areas are defined as the "1" and "2" areas. (b) Vertical profiles of the averaged vorticity anomalies over significant areas in (a). (c) Spatial distribution of the 250-hPa meridional wind (units: m s^{-1}) under the vorticity forcing in the LBM experiment. The green box indicates the location of NWC.

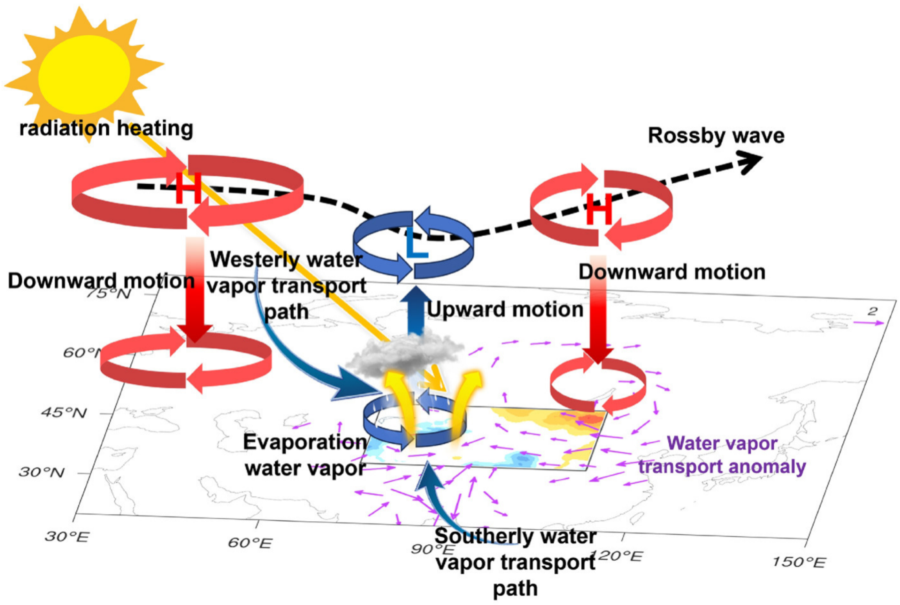

Fig. 13. A schematic diagram illustrating the mechanisms responsible for the humidification in NWC.

improving water vapor source tracking models to more accurately estimate the contributions from different water vapor sources and investigate how interactions between high-altitude and low-altitude wind fields influence water vapor transport pathways and precipitation patterns. Recent evidence indicates that low-frequency variations of moisture transport into Central Asian drylands are mainly determined by circulation changes (Zhong et al., 2021, 2022), reinforcing the need for three-dimensional diagnostics that explicitly resolve vertical shear.

Previous studies have generally predicted that the humidification trend in NWC may persist (Jiang et al., 2020; Yang et al., 2021; Chen et al., 2023). However, our findings clearly indicate that the increased atmospheric moisture is primarily sustained by enhanced local evapotranspiration. This increase in evapotranspiration is largely driven by accelerated local glacier and snow melt (Chen et al., 2023). The rising temperatures have accelerated glacier snowmelt, temporarily increasing the surface water supply. When the finite glacier reserves are consumed, the local evapotranspiration that supports the humidification will inevitably be weakened. Furthermore, the AMO is currently in its positive phase, which enhances precipitation in NWC. When the AMO inevitably shifts to its negative phase, its influence will counteract the background precipitation increase response to global warming, leading to a significant weakening or even reversal of the humidification trend. Therefore, the humidification is systemically constrained by an unsustainable water source due to the primary moisture input mechanism and the phase change of interdecadal variability. Both factors indicate that the humidification of NWC is unlikely to be sustained in the future. The previous studies that project persistent humidification probably overestimate the response of precipitation to global warming and underestimate the role of internal variability.

Predicting the future sustainability of the humidification of NWC remains a major challenge, primarily due to uncertainties surrounding the timing of the AMO's phase shift and its complex interaction with global warming. Current climate models face significant difficulties in predicting the internal variability, especially the phase transitions of AMO, which hinder reliable precipitation predictability. Future research should prioritize developing predictive frameworks that integrate dynamic mechanisms with statistical relationships, combining insights from observational data and numerical simulations. Improving the prediction of AMO phase transitions and associated precipitation variability is a critical and challenging frontier. Such advancements are essential for forecasting future hydrological shifts in the drylands.

Acknowledgements. This work was jointly supported by the National Natural Science Foundation of China (U2442207), the Youth Innovation Promotion Association of the Chinese Academy of Sciences (2021427), the West Light Foundation (xbzg-zdsys-202409) of the Chinese Academy of Sciences, Central Guidance Fund for Local Science, and Technology Development Projects in Gansu (Grant No. 24ZYQA031). We acknowledge the Computing Center in Xi'an for providing the computing resources.

Conflict of Interest. The authors declare no conflicts of interest relevant to this study.

REFERENCES

Brubaker, K. L., D. Entekhabi, and P. S. Eagleson, 1993: Estimation of continental precipitation recycling. *J. Climate*, **6**(6), 1077−1089, https://doi.org/10.1175/1520-0442(1993)006<1077:EOCPR>2.0.CO;2.

Burde, G. I., A. Zangvil, and P. J. Lamb, 1996: Estimating the role of local evaporation in precipitation for a two-dimensional region. *J. Climate*, **9**, 1328−1338, https://doi.org/10.1175/1520-0442(1996)009<1328:ETROLE>2.0.CO;2.

Chen, C. Z., X. J. Zhang, H. Y. Lu, L. Y. Jin, Y. Du, and F. H. Chen, 2021a: Increasing summer precipitation in arid central Asia linked to the weakening of the East Asian summer monsoon in the recent decades. *Int. J. Climatol.*, **41**(2), 1024−1038, https://doi.org/10.1002/joc.6727.

Chen, D. D., and Y. J. Dai, 2009: Characteristics of northwest China rainfall intensity in recent 50 years. *Chinese J. Atmospheric Sci.*, **33**(5), 923−935, https://dx.doi.org/10.3878/j.issn.1006-9895.2009.05.04. (in Chinese)

Chen, F. H., J. Chen, and W. Huang, 2021b: Weakened East Asian summer monsoon triggers increased precipitation in Northwest China. *Sci. China Earth Sci.*, **64**(5), 835−837. https://doi.org/10.1007/s11430-020-9731-7.

Chen, F. H., T. T. Xie, Y. J. Yang, S. Q. Chen, F. Chen, W. Huang, and J. Chen, 2023: Discussion of the "warming and wetting" trend and its future variation in the drylands of Northwest China under global warming. *Sci. China Earth Sci.*, **66**, 1241−1257, https://doi.org/10.1007/s11430-022-1098-x.

Chen, G. S., and R. H. Huang, 2012: Excitation mechanisms of the teleconnection patterns affecting the July precipitation in Northwest China. *J. Climate*, **25**(22), 7834−7851, https://doi.org/10.1175/JCLI-D-11-00684.1.

Chen, Y., and P. M. Zhai, 2014: Two types of typical circulation pattern for persistent extreme precipitation in Central-Eastern China. *Quart. J. Roy. Meteor. Soc.*, **140**, 1467−1478, https://doi.org/10.1002/qj.2231.

Chou, C., and C. W. Lan, 2012: Changes in the annual range of precipitation under global warming. *J. Climate*, **25**(1), 222−235, https://doi.org/10.1175/JCLI-D-11-00097.1.

Christidis, N., and P. A. Stott, 2021: The influence of anthropogenic climate change on wet and dry summers in Europe. *Sci. Bull.*, **66**, 813−823, https://doi.org/10.1016/j.scib.2021.01.020.

Dominguez, F., P. Kumar, X. Z. Liang, and M. Ting, 2006: Impact of atmospheric moisture storage on precipitation recycling. *J. Climate*, **19**(8), 1513−1530, https://doi.org/10.1175/JCLI3691.1.

Dominguez, F., H. Hu, and J. A. Martinez, 2020: Two-layer dynamic recycling model (2L-DRM): Learning from moisture tracking models of different complexity. *J. Hydrometeorol.*, **21**(1), 3−16, https://doi.org/10.1175/JHM-D-19-0101.1.

Dore, M. H. I., 2005: Climate change and changes in global precipitation patterns: What do we know. *Environ. Int.*, **31**, 1167−1181, https://doi.org/10.1016/j.envint.2005.03.004.

Gong, Z. Q., G. L. Feng, M. M. Dogar, and G. Huang, 2018: The possible physical mechanism for the EAP–SR co-action. *Climate Dyn.*, **51**(4), 1499−1516, https://doi.org/10.1007/s00382-017-3967-4.

Harris, I., T. J. Osborn, P. Jones, and D. Lister, 2020: Version 4 of the CRU TS monthly high-resolution gridded multivariate climate dataset. *Sci. Data*, **7**(1), 109, https://doi.org/10.1038/s41597-020-0453-3.

Held, I. M., and B. J. Soden, 2006: Robust responses of the hydrological cycle to global warming. *J. Climate*, **19**(21), 5686−5699, https://doi.org/10.1175/JCLI3990.1.

Herrera-Estrada, J. E., J. A. Martinez, F. Dominguez, K. L. Findell, E. F. Wood, and J. Sheffield, 2019: Reduced moisture transport linked to drought propagation across North America. *Geophys. Res. Lett.*, **46**, 5243–5253, https://doi.org/10.1029/2019GL082475.

Hsu, P. C., T. Li, and B. Wang, 2011: Trends in global monsoon area and precipitation over the past 30 years. *Geophys. Res. Lett.*, **38**, L08701, https://doi.org/10.1029/2011GL046893.

Hu, Q., Y. Zhao, A. N. Huang, P. Ma, and J. Ming, 2021: Moisture transport and sources of the extreme precipitation over northern and southern Xinjiang in the summer half-year during 1979–2018. *Front. Earth Sci.*, **9**, 770877, https://doi.org/10.3389/feart.2021.770877.

Hua, L. J., L. H. Zhong, and Z. G. Ma, 2017: Decadal transition of moisture sources and transport in Northwestern China During summer from 1982 to 2010. *J. Geophys. Res.: Atmos.*, **122**, 12 499–13 078, https://doi.org/10.1002/2017JD027728.

IPCC, 2021: *Climate Change 2021 – The Physical Science Basis. Contribution of Working Group I to the Sixth Assessment Report of the Intergovernmental Panel on Climate Change*. Cambridge University Press.

Jiang, J., T. J. Zhou, X. L. Chen, and L. X. Zhang, 2020: Future changes in precipitation over central Asia based on CMIP6 projections. *Environ. Res. Lett.*, **15**(5), 054009, https://doi.org/10.1088/1748-9326/ab7d03.

Jin, C. H., B. Wang, and J. Liu, 2020: Future changes and controlling factors of the eight regional monsoons projected by CMIP6 models. *J. Climate*, **33**(21), 9307–9326, https://doi.org/10.1175/JCLI-D-20-0236.1.

Kobayashi, S., and Coauthors, 2015: The JRA-55 reanalysis: General specifications and basic characteristics. *J. Meteor. Soc. Japan*, **93**, 5–48, https://doi.org/10.2151/jmsj.2015-001.

Kosaka, Y., and H. Nakamura, 2006: Structure and dynamics of the summertime Pacific–Japan teleconnection pattern. *Quart. J. Roy. Meteor. Soc.*, **132**(619), 2009–2030, https://doi.org/10.1256/qj.05.204.

Lettau, H., K. Lettau, and L. C. B. Molion, 1979: Amazonia's hydrologic cycle and the role of atmospheric recycling in assessing deforestation effects. *Mon. Wea. Rev.*, **107**(3), 227–238, https://doi.org/10.1175/1520-0493(1979)107<0227:AHCATR>2.0.CO;2.

Li, M. X., and Z. G. Ma, 2018: Decadal changes in summer precipitation over arid northwest China and associated atmospheric circulations. *Int. J. Climatol.*, **38**(12), 4496–4508, https://doi.org/10.1002/joc.5682.

Li, M. Y., D. H. Luo, Y. Yao, and L. H. Zhong, 2020: Large-scale atmospheric circulation control of summer extreme hot events over China. *Int. J. Climatol.*, **40**, 1456–1476, https://doi.org/10.1002/joc.6279.

Li, Y. P., Y. N. Chen, and Z. Li, 2019: Dry/wet pattern changes in global dryland areas over the past six decades. *Glob. Planet. Change*, **178**, 184–192, https://doi.org/10.1016/j.gloplacha.2019.04.017.

Liu, J., F. Liu, D. Tuoliewubieke, and L. M. Yang, 2020a: Analysis of the water vapour transport and accumulation mechanism during the "7.31" extreme rainstorm event in the southeastern Hami area, China. *Meteor. Appl.*, **27**(4), e1933, https://doi.org/10.1002/met.1933.

Liu, Y., W. Zhou, X. Qu, and R. G. Wu, 2020b: An interdecadal change of the boreal summer Silk Road Pattern around the late 1990s. *J. Climate*, **33**(16), 7083–7100, https://doi.org/10.1175/JCLI-D-19-0795.1.

Lu, S., Z. Y. Hu, H. P. Yu, W. W. Fan, C. W. Fu, and D. Wu, 2021: Changes of extreme precipitation and its associated mechanisms in Northwest China. *Adv. Atmos. Sci.*, **38**, 1665–1681, https://doi.org/10.1007/s00376-021-0409-3.

Martinez, J. A., and F. Dominguez, 2014: Sources of atmospheric moisture for the La Plata River basin. *J. Climate*, **27**, 6737–6753, https://doi.org/10.1175/JCLI-D-14-00022.1.

Mattingly, K. S., C. A. Ramseyer, J. J. Rosen, T. L. Mote, and R. Muthyala, 2016: Increasing water vapor transport to the Greenland Ice Sheet revealed using self-organizing maps. *Geophys. Res. Lett.*, **43**, 9250–9258, https://doi.org/10.1002/2016GL070424.

Ning, G. C., and Coauthors, 2021: Understanding the mechanisms of summer extreme precipitation events in Xinjiang of arid Northwest China. *J. Geophys. Res.: Atmos.*, **126**, e2020JD034111, https://doi.org/10.1029/2020JD034111.

Qin, M. H., D. L. Li, A. G. Dai, W. J. Hua, and H. D. Ma, 2018: The influence of the pacific decadal oscillation on north central China precipitation during boreal autumn. *Int. J. Climatol.*, **38**, e821–e831, https://doi.org/10.1002/joc.5410.

Ren, Y., and Coauthors, 2022: Attribution of dry and wet climatic changes over Central Asia. *J. Climate*, **35**(5), 1399–1421, https://doi.org/10.1175/JCLI-D-21-0329.1.

Sardeshmukh, P. D., and B. J. Hoskins, 1988: The generation of global rotational flow by steady idealized tropical divergence. *J. Atmos. Sci.*, **45**(7), 1228–1251, https://doi.org/10.1175/1520-0469(1988)045<1228:TGOGRF>2.0.CO;2.

Schär, C., D. Lüthi, U. Beyerle, and E. Heise, 1999: The soil–precipitation feedback: A process study with a regional climate model. *J. Climate*, **12**(3), 722–741, https://doi.org/10.1175/1520-0442(1999)012<0722:TSPFAP>2.0.CO;2.

Seager, R., and G. A. Vecchi, 2010: Greenhouse warming and the 21st century hydroclimate of southwestern North America. *Proceedings of the National Academy of Sciences of the United States of America*, **107**(50), 21 277–21 282, https://doi.org/10.1073/pnas.0910856107.

Seager, R., N. Naik, and G. A. Vecchi, 2010: Thermodynamic and dynamic mechanisms for large-scale changes in the hydrological cycle in response to global warming. *J. Climate*, **23**(17), 4651–4668, https://doi.org/10.1175/2010JCLI3655.1.

Seager, R., N. Naik, and L. Vogel, 2012: Does global warming cause intensified interannual hydroclimate variability? *J. Climate*, **25**(9), 3355–3372, https://doi.org/10.1175/JCLI-D-11-00363.1.

Shi, J. Q., Y. Yao, R. W. Guo, B. H. Luo, and L. H. Zhong, 2025: The intensifying relationship between heatwaves in the mid-lower reaches of the Yangtze River valley and the upstream atmospheric wave train after the 2000s. *Atmos. Res.*, **313**, 107770, https://doi.org/10.1016/j.atmosres.2024.107770.

Shi, Y. F., Y. P. Shen, E. S. Kang, D. L. Li, Y. J. Ding, G. W. Zhang, and R. J. Hu, 2007: Recent and future climate change in northwest China. *Clim. Change*, **80**, 379–393, https://doi.org/10.1007/s10584-006-9121-7.

Trenberth, K. E., 1998: Atmospheric moisture residence times and cycling: Implications for rainfall rates and climate change. *Clim. Change*, **39**, 667–694, https://doi.org/10.1023/A:1005319109110.

Trenberth, K. E., 2011: Changes in precipitation with climate change. *Climate Res.*, **47**, 123–138, https://doi.org/10.3354/cr00953.

Trenberth, K. E., and D. J., Shea, 2006: Atlantic Hurricanes and

Natural Variability in 2005. *Geophys. Res. Lett.*, **33**, L12704, https://doi.org/10.1029/2006gl026894.

Van Der Ent, R. J., and H. H. G. Savenije, 2013: Oceanic sources of continental precipitation and the correlation with sea surface temperature. *Water Resour. Res.*, **49**, 3993–4004, https://doi.org/10.1002/wrcr.20296.

Wang, Q., P. M. Zhai, and D. H. Qin, 2020: New perspectives on "warming–wetting" trend in Xinjiang, China. *Adv. Clim. Change Res.*, **11**(3), 252–260, https://doi.org/10.1016/j.accre.2020.09.004.

Wang, S. J., M. J. Zhang, Y. J. Che, F. L. Chen, and F. Qiang, 2016: Contribution of recycled moisture to precipitation in oases of arid central Asia: A stable isotope approach. *Water Resour. Res.*, **52**(4), 3246–3257, https://doi.org/10.1002/2015WR018135.

Wang, S. S., J. P. Huang, Y. L. He, and Y. P. Guan, 2014: Combined effects of the pacific decadal oscillation and el Niño-southern oscillation on global land dry-wet changes. *Sci. Rep.*, **4**(1), 6651, https://doi.org/10.1038/srep06651.

Wang, S. S., J. P. Huang, G. Huang, F. Luo, Y. L. Ren, and Y. L. He, 2022: Enhanced impacts of Indian Ocean sea surface temperature on the dry/wet variations over Northwest China. *J. Geophys. Res.: Atmos.*, **127**(11), e2022JD036533, https://doi.org/10.1029/2022JD036533.

Wang, X. Y., M. Xu, S. C. Kang, X. M. Li, H. D. Han, and X. D. Li, 2024: Comprehensive applicability evaluation of four precipitation products at multiple spatiotemporal scales in Northwest China. *J. Arid Land*, **16**, 1232–1254, https://doi.org/10.1007/s40333-024-0084-1.

Watanabe, M., and M. Kimoto, 2000: Atmosphere-ocean thermal coupling in the North Atlantic: A positive feedback. *Quart. J. Roy. Meteor. Soc.*, **126**(570), 3343–3369, https://doi.org/10.1002/qj.49712657017.

Wu, P., Y. H. Ding, Y. J. Liu, and X. C. Li, 2019: The characteristics of moisture recycling and its impact on regional precipitation against the background of climate warming over Northwest China. *Int. J. Climatol.*, **39**(14), 5241–5255, https://doi.org/10.1002/joc.6136.

Wu, P., Y. J. Liu, Y. H. Ding, X. C. Li, and J. Wang, 2022: Modulation of sea surface temperature over the North Atlantic and Indian-Pacific warm pool on interdecadal change of summer precipitation over Northwest China. *Int. J. Climatol.*, **42**(16), 8526–8538, https://doi.org/10.1002/joc.7743.

Xu, P., L., L. Wang, and W. Chen, 2019: The British–Baikal Corridor: A teleconnection pattern along the summertime polar front jet over Eurasia. *J. Climate*, **32**, 877–896, https://doi.org/10.1175/JCLI-D-18-0343.1.

Xue, T., Y. H. Ding, and C. H. Lu, 2022: Interdecadal variability of summer precipitation in northwest China and associated atmospheric circulation changes. *J. Meteor. Res.*, **36**(6), 824–840, https://doi.org/10.1007/s13351-022-2021-6.

Yang, J. H., Q. Zhang, X. Y. Liu, P. Yue, J. L. Shang, H. Ling, and W. J. Li, 2019: Spatial-temporal characteristics and causes of summer precipitation anomalies in the transitional zone of typical summer monsoon, China. *Chinese J. Geophys.*, **62**, 4120–4128, https://doi.org/10.6038/cjg2019M0639. (in Chinese)

Yang, X. L., B. T. Zhou, Y. Xu, and Z. Y. Han, 2021: CMIP6 Evaluation and Projection of Temperature and Precipitation over China. *Adv. Atmos. Sci.*, **38**, 817–830, https://doi.org/10.1007/s00376-021-0351-4.

Yao, J. Q., Y. N. Chen, Y. Zhao, X. F. Guan, W. Y. Mao, and L. M. Yang, 2020: Climatic and associated atmospheric water cycle changes over the Xinjiang, China. *J. Hydrol.*, **585**, 124823, https://doi.org/10.1016/j.jhydrol.2020.124823.

Yao, S. B., D. B. Jiang, and Z. S. Zhang, 2021: Moisture sources of heavy precipitation in Xinjiang characterized by meteorological patterns. *J. Hydrometeorol.*, **22**(8), 2213–2225, https://doi.org/10.1175/JHM-D-20-0236.1.

Zhang, J. X., S. S. Wang, Y. L. He, Y. Ren, and J. P. Huang, 2022a: Contribution of the precipitation-recycling process to the wetting trend in Xinjiang, China. *J. Geophys. Res.: Atmos.*, **127**(11), e2021JD036407, https://doi.org/10.1029/2021JD036407.

Zhang, Q., J. J. Lin, W. C. Liu, and L. Y. Han, 2019: Precipitation seesaw phenomenon and its formation mechanism in the eastern and western parts of Northwest China during the flood season. *Sci. China Earth Sci.*, **62**(12), 2083–2098, https://doi.org/10.1007/s11430-018-9357-y.

Zhang, Q., and Coauthors, 2021: Climatic warming and humidification in the arid region of Northwest China: Multi-scale characteristics and impacts on ecological vegetation. *J. Meteor. Res.*, **35**, 113–127, https://doi.org/10.1007/s13351-021-0105-3.

Zhang, Q., and Coauthors, 2022b: The eastward expansion of the climate humidification trend in northwest China and the synergistic influences on the circulation mechanism. *Climate Dyn.*, **59**, 2481–2497, https://doi.org/10.1007/s00382-022-06221-4.

Zheng, Z. Y., Z. G. Ma, M. X. Li, and J. J. Xia, 2017: Regional water budgets and hydroclimatic trend variations in Xinjiang from 1951 to 2000. *Clim. Change*, **144**(3), 447–460, https://doi.org/10.1007/s10584-016-1842-7.

Zhong, L. H., L. J. Hua, and D. H. Luo, 2018: Local and external moisture sources for the arctic warming over the Barents–Kara Seas. *J. Climate*, **31**, 1963–1982, https://doi.org/10.1175/JCLI-D-17-0203.1.

Zhong, L. H., L. J. Hua, Y. Yao, and J. M. Feng, 2021: Interdecadal aridity variations in Central Asia during 1950–2016 regulated by oceanic conditions under the background of global warming. *Clim. Dynam.*, **56**, 3665–3686, https://doi.org/10.1007/s00382-021-05659-2.

Zhong, L. H., L. J. Hua, Z. H. Gong, Y. Yao, and L. Mu, 2022: Quantifying the spatial characteristics of the moisture transport affecting precipitation seasonality and recycling variability in Central Asia. *Adv. Atmos. Sci.*, **39**, 967–984, https://doi.org/10.1007/s00376-021-1383-5.

Zhou, B. Q., and P. M. Zhai, 2016: A new forecast model based on the analog method for persistent extreme precipitation. *Wea. Forecasting*, **31**, 1325–1341, https://doi.org/10.1175/WAF-D-15-0174.1.

Zhou, Y. S., Z. M. Xie, and X. Liu, 2019: An analysis of moisture sources of torrential rainfall events over Xinjiang, China. *J. Hydrometeorol.*, **20**(10), 2109–2122, https://doi.org/10.1175/JHM-D-19-0010.1.

Zhu, Y. L., H. J. Wang, J. H. Ma, T. Wang, and J. Q. Sun, 2015: Contribution of the phase transition of pacific decadal oscillation to the late 1990s' shift in East China Summer Rainfall. *J. Geophys. Res. -Atmos.*, **120**(17), 8817–8827, https://doi.org/10.1002/2015JD023545.